Erosion mode and history of Eastern Adamaoua landscapes (Cameroon): Superimposed lateritic weathering of granites and basalts

Mathieu Nouazi Momo, Anicet Beauvais, Gatien Romuald Kenfack Nguemo, Ethel Nkongho Ashukem, Edima Roland Yana, Salomon César Nguemhe-Fils, Rachel Ngo Nyouma, Alex Chimeu Akaba

Erosion mode and history of Eastern Adamaoua landscapes (Cameroon): Superimposed lateritic weathering of granites and basalts

Mathieu Nouazi Momo[1], Anicet Beauvais[2], Gatien Romuald Kenfack Nguemo[3], Ethel Nkongho Ashukem[1], Edima Roland Yana[1], Salomon César Nguemhe-Fils[1], Rachel Ngo Nyouma[1], Alex Chimeu Akaba[4]

[1] Institute of Geological and Mining Research (IRGM), P.O. Box 4110 Yaoundé, Cameroon

[2] Aix-Marseille Univ, CNRS, IRD, INRAE, CEREGE, BP 80, 13545, Aix-en-Provence, Cedex 4, France

[3] University of Dschang, Faculty of Science - Department of Earth Sciences. PO Box 67 Dschang - Cameroon

[4] University of Yaoundé 1, Faculty of Science, Department of Earth Sciences. PO Box 337 Yaoundé, Cameroon

https://doi.org/10.1016/j.catena.2023.107071

*Corresponding author Email: nouazimat@yahoo.fr

Abstract

Landscapes of eastern Adamaoua highlands have been shaped by successive weathering and erosion processes of Pan-African crystalline rocks and Neogene volcanics cover. Basalts have outpoured through major inherited structural discontinuities mostly in shallow incisions of lateritic pediplains previously shaped on the granitic basement. That has resulted in formation of a singular composite lateritic weathering profile on basalt superimposed to a truncated profile composed of mottled clays and saprolite on granite. The composite profile studied here is little evolved, mostly kaolinised on granite while basalt is weakly to moderately lateritised owing to differences in silica and iron oxide contents of the two contrasted parent rocks. During lateritic weathering, Cu, Ni, and Co are enriched in profile on granite but depleted on basalt, while Zr/Ti is relatively constant. Behavior and fractionation of REE are comparable except higher Eu* and Ce* anomaly on granite profile than on weathered basalt, owing to parent minerals differences, mostly feldspars in granite versus plagioclase and Fe-Mg minerals in basalt. The contrast in Eu* is also linked to differences in the Index Of Laterization (IOL) in weathered horizons of the two parent rocks. Beyond quite classical litho-dependent geochemical differences in the composite profile, persistence of per-humid climate and good drainage over Neogene have sustained rock-weathering and local surface erosion processes upon volcanic outpours and their contact surface with pediplains formed on Pan-African granitoids of Adamaoua highland.

Keywords: Lateritic weathering; Erosion; Granite; Basalt; Neogene; Cameroon.

1. Introduction

Lateritic landscape dynamics and formation of lateritic profiles on tectonically-stable cratonic continental platforms across tropical belts have been primarily driven by climatic and lithologic factors that constrained the amplitude of weathering, erosion and geomorphic processes over Paleogene (Thomas, 1994; Tardy and Roquin, 1998; Colin et al., 2005; Beauvais et al, 2008; Beauvais and Chardon, 2013; Beauvais et al., 2016; Chardon et al., 2018; Vasconcelos and Carmo, 2018; Jean et al., 2020). West African lateritic paleo-landscapes, whose relics are currently preserved for million years in West Africa (Beauvais and Chardon, 2013) have formed under Paleocene – Eocene humid climates but afterward evolved under post-Eocene drying climatic conditions across the West African platform (e.g., Chardon et al., 2018). Once swells like the Jos plateau plateau in Nigeria and the Adamaoua highland in Cameroon have established under Paleocene - Eocene epirogenic uplift driven by under-plating mantle activity (Burke, 2001), lateritic rock weathering process have operated on the uplifted surfaces. Afterwards, lateritic paleo-landscapes evolved under long-lasting humid climatic conditions (post-Eocene to late Neogene) that effectively prevailed upon these uplifted platforms. Long-term preservation of lateritic paleosurfaces and regolith formed on granitic basements depends on weathering and erosion processes intensity, which have been differentially mostly amplified by major trajectories of climatic regimes and the possible effects of eventual tectonics. For example, these factors combined together may have induced deformation of previously formed paleo-landscapes and their drainage networks across and around intra-cratonic swells (Burke and Gunnell, 2008; Grimaud et al., 2014; Chardon et al., 2016).

The ancient lateritic landscapes (mainly pediplains) formed on the Pan-African basement in Adamaoua mainly evolved under persistent humid climatic regimes during the middle and late Cenozoic. Neogene basaltic flows outpoured over the pediplains through

major structural discontinuities, and their lateritic weathering has completed the edification of composite profiles. Nguetnkam et al., (2020) described paleosols and saprolite on granite and superimposed basalts, respectively, and interpreted the current lateritic profile edifice as the result of local relief inversion of a previous valley on granite filled by late Neogene basalts. Eventual tectonic effect of basalt outpourings (among other volcanics) on landscape incision remains however a matter of debate that is out of the scope of this paper. Here, we document the history and erosion mode of Eastern Adamaoua landscape by describing in details the formation of such a composite lateritic profile on the basis of major petro-geochemical evolution paths across that profile, complemented by regional scale field observations on geomorphological surfaces and regolith types on granite and basalt in and around the studied profile. We considered the major influence of long-lasting per-humid climatic conditions on the geochemical differentiation and elements fractionation across the lateritic profiles formed on the different lithologies and upon the landscape erosion pattern of eastern Adamaoua highland. The known ages (~9 to ~11 Ma; see Marzoli et al., 1999) of basaltic flows over lateritic pediplains previously formed on granite basement impose a relative chronology of weathering and landscape erosion. Our study opens perspectives to larger scale analysis of volcanically-driven regolith geomorphological markers that seal the minimum age of underneath lateritic pediplains on Adamaoua highlands.

2. Major geological and geomorphological features of Eastern Adamaoua

The granitoid basement of the Adamaoua plateau belongs to the Pan-African orogenic belt of Central Africa ($^{207}Pb/^{206}Pb$ zircon ages of ~ 500-600 Ma, Ganwa et al., 2011). Pulses of volcanic activities with evidences of mantle sources (lherzolites, Girod et al., 1984) resulted in establishment of strato-volcanos (~ 400 m, Marzolli et al., 2000) upon previously-formed lateritic sequences on granitoids, in eastern Adamaoua highland (Figs. 1a-b). Basalts

outpoured through structural discontinuities (opened faults and fractures) inherited from post-orogenic distensile tectonics that affected the Pan-African basement of Adamaoua (Deruelle et al., 1991). Detailed chronological and petrological studies revealed successive stages of volcanic activities (Marzoli et al., 1999, 2000; Delor et al., 2021). Voluminous stratoïd alkaline basalts and basanites at c. 11 Ma, are then covered, from 11 Ma to 9 Ma, by silicic magmas extrusions mainly nepheline-rich trachytes (Marzoli et al., 1999) with spots of rhyolites and phonolites (Lasserre, 1961) at Tchabal Nghana (Fig. 1a). A last stage is represented by minor basaltic flows and pyroclastic deposits dating from Quaternary (Kagou Ndongmo et al., 2010). The wide age range from Miocene to Quaternary is suggestive of multiple magmatic hot-spots operating beneath the Cameroon Volcanic line (Marzolli et al., 1999; 2000).

Low-relief lateritic landscapes are marked by a NW sloping regional composite surface on granitoids and volcanics (Fig. 1b). On syn-tectonic granites, lateritic pediments form kilometers wide rolling pediplain between c. 1200 m a.s.l. to c. 1420 m a.s.l (Fig. 1b), which are interrupted by c. 40 m height hills of poorly weathered recent basalts/basanites (Fig. 2a). Lateritic duricrusts formed on pediments at c. 1200 m altitude show a composite assemblage of nodular and massive ferricretes (Fig. 2b). At higher altitudes, hillsides of truncated weathering profiles on pediments are covered by saprolites or sandy mottled clays.

Scarped erosion slopes mark major lithological unconformity between the upper pediplain on syn-tectonic granites and the lower pediment surface on migmatites and gneiss (Fig. 1b). This is linked to a regional extension of a faulting system N70°E that established on the Adamaoua highland as a result of Albian-Cenomanian extensive tectonic (Allix et al., 1984) with major lithological control (see Fig. 1). Below the scarped slope at c. 1100 m a.s.l. (Fig. 1b), piedmont surfaces are covered by ferricrete (Figs. 2c-d).

In contrast to landscape on granitoids, landsurfaces on mid-Miocene basalts are marked by a succession of smoothed hills covered by consolidated ferricretes/bauxites, that are dismantled mostly on the edges of eroded plateaus (Fig. 2e), which the incision led to the formation of a lower and younger pediment surface (Fig. 2f).

3. Methodological approach

Field geomorphological observations at regional scale (Fig. 1a) allowed to characterize lateritic landsurfaces deriving from lateritic weathering of granitoids and basalts, and landscape dissection (Fig. 1b). This detailed geomorphic characterization was undertaken along a NW-SE prospect in area exposing a patchwork of multiple weathered volcanic covers and surfaces of lateritic pediplains formed on granite. Field stations (Fig. 1a) were chosen to also analyze the broader ranges of altitudes in the studied area (Fig. 1b) including a major structural discontinuity of the Adamaoua that may constrain the lateritic surfaces distribution. At a given field station, elevations and petrographic descriptions of preserved regolith/duricrusts on granite or basalts were recorded and linked to specific landscape morphology.

Based on a detailed geological map (Lasserre, 1961), field survey allowed to determine outcrops of composite weathering profiles, that are arranged preferably around geological contacts between crystalline basement and overlying lavas flows, e.g. Mangoli (see Nguetnkam et al., 2020, and this study, Fig. 1). A road trench exposing 35° NW-dipping structures permitted to describe the weathering profile MEI01 and its different horizons formed on granite and basalt (Fig. 3a). The composite weathering profile exemplified regional scale regolith formed on low-reliefs lateritic pediplains and erosional slopes on granitoids, which have been then covered by mid- to late Miocene volcanics (basalts and/or andesites)

143 before renewed weathering and laterization under propitious climatic conditions over the late
144 Neogene.

145 Eleven samples including the two parent rocks (granite and basalt) were collected in
146 the different horizons of the weathering profile section (Fig. 3a). Weathered samples were
147 described according to reference nomenclature of Nahon (1991) and Tardy (1997), while their
148 dominant hue was estimated using codes from the Munsell color chart (Mc).

149 Samples were prepared and analyzed by the ALS Laboratory Group SL, Spain.
150 Samples were crushed to a sieved size of 2 mm that underwent further pulverization such that
151 more than 85% of grounded sample be sieved to 75 µm. Prior to 4 acid dissolution and ICP-
152 MS analysis, the lithium borate fusion was applied to samples, that is suited for quantitative
153 analyze of whole rock elements. The quality control here is based on a number of blanks,
154 reference materials (standards) and duplicates that are analyzed along with the samples. The
155 ICPMS (Inductively coupled plasma-Mass spectrometry) method was used for analyzing a
156 combination of Major (wt.%), Trace and Rare Earth elements in ppm (ME-MS81^{TM} + whole
157 rock package ME-ICP06; www.alsglobal.com). The detection limits of each element are
158 given in the table 1 caption, table 2 and 3.

159 The geochemical Index Of Laterization, IOL, was also calculated for better
160 understanding and comparing lateritic weathering processes intensity in each section of the
161 composite profile. The IOL considers major elements, Al, Si and Fe, involved in the lateritic
162 processes such as:

163

164 $$IOL = 100 \times \left[\frac{(Al_2O_3 + Fe_2O_3)}{(SiO_2 + Al_2O_3 + Fe_2O_3)} \right] \quad (1)$$

165

166 The IOL values were then reported on a scale alongside a ternary diagram (SiO_2-
167 Al_2O_3-Fe_2O_3), which allow to distinguishing different laterization grades (Schellmann, 1994;
168 see also Babechuk et al., 2014).
169
170 **4. Results**
171 4.1. Petrological differentiations across the composite profile
172 The profile is composed of weathering horizons formed on granite and overlying
173 basalt defining two sections separated by an inconformity marking a rippled contact (Fig. 3a),
174 which dips ca. 35° roughly parallel to surface slope gradient toward the local valley incision
175 to the NW. From the bottom to the top of the profile on granite, a ca. 4 m thick nodular
176 horizon M1g is overlaid by a 3.3 m thick mottled clay M2g on granite, while a 2.4 m thick
177 mottled clay M1b topped by 2.3 m thick pebbly horizon compose the profile on basalt (Fig.
178 3).
179 Granite (Fig. 4a) is composed of quartz, feldspars, amphiboles and biotites. Blocks of
180 granite also outcrop in river beds and are widespread in adjacent lowlands where lateritic
181 regolith has been stripped. At the bottom of the profile, the nodular horizon (M1g) is made up
182 of a brown-reddish clay-ferruginous matrix (Mc: 2.5 YR 4/8) embedding few nodules with
183 some preserved centimeter-sized whitish saprolitic relics (Fig. 4b). In higher part of this
184 horizon (Fig. 3b), numerous pluri-centimeter sized dark-red nodules (Mc: 10R 3/6) are
185 embedded in a reddish (Mc: 2.5 YR 3/5) friable internodular matrix (Fig. 4c); the horizon is
186 limited upward by a centimeter-sized dark brown crusting (Fig. 3a-b). The overlying
187 yellowish-red (Mc: 5YR 4/5) mottled clays (M2g) are formed in-situ. The upper part is made
188 up of a yellowish-red to yellow clay-ferruginous matrix (Mc: 7.5 YR 7/6) studded with quartz
189 grains (Fig. 4d). The lower part of M2g shows the original structure of the fresh granite rock
190 crossed by a network of fractures marked by iron crystallizations coating (Figs. 3a-b and 4e).

Basalt coarse structure is preserved in the upper section of the weathering profile with a columnar-jointed vertical network in the mottled clays horizon (Figs. 3d). Basalt is dark grey massive and microcrystalline (Fig. 5a), with some phenocrysts of olivines and pyroxenes observed under a magnifying glass. The base of the profile on basalt is made up of a yellowish (Mc: 7.5 YR 7/6) mottled clay horizon (M1b), which shows a sharp transition with the underlying horizons on granite (Fig. 3c). This horizon is massive and made up of undifferentiated yellowish clay studded with preserved structures of micrometric inherited primary minerals, and crossed by centimeter sized voids filled with a dark brown (Mc: 7.5 YR 5/5) loose fine earth (Fig. 5b). The basaltic structure is progressively indistinct in the pebbly horizon M2b composed of 70% pebbles and 30 % fine earth (Fig. 5c).

4.2. Major and trace elements across the composite profile

Graphical distributions of major elements and IOL values are showed in figures 6 (see also analyses in Tab. 1). Data analysis highlights decreasing SiO_2 content and increasing contents of Fe_2O_3 and Al_2O_3 relative to the respective parent rocks (Fig. 6). The maximum depletion of SiO_2 and element enrichment of Fe_2O_3 occur at the top of the nodular horizon (M1g) on granite (Figs. 6 and 7a).

Laterization index IOL progressively increases from parent rocks to kaolinized weathering horizons on granite, and to weakly and moderately lateritised horizons on basalt (Fig. 6; see also Tab. 1).

Trace elements behavior relative to parent rocks are given in the figure 7 (see also Tab. 2) and their relations to each other and major elements in figures 8. Ba, Rb, Sr and Zr are the most abundant trace elements in the granite with up to 1035 ppm for Ba (Tab. 2); trace elements in weathering horizons are further enriched relative to the granite except Sr, Rb, Ba, Y and Zn, which are depleted (Fig. 7a). Nb, Zr, Ga, Cu, Ni, Co, Cr, V, Sc, Th, Hf, U and Ta

contents increase from the fresh granite to the top of the lower section of the profile (Fig. 7a; Tab. 2) and vary together in the weathering horizons (e.g., $r^2_{Cr\text{-}Th}$=0.81; Fig. 8a-b). Trace elements are also IOL dependent with a significant enrichment with increasing laterization (e.g., $r^2_{IOL\text{-}Th}$=0.98; Fig. 8c-d). Their distribution in the section is linked to major oxides like TiO_2, Al_2O_3, and Fe_2O_3 to some extent (e.g., $r^2_{Ni\text{-}Al2O3}$=0.90; Fig. 8e-h).

In the upper litho-section of the profile on basalt, Nb, Y, Sr, Ba, Zn, Ni, Co and Sc are the most abundant trace elements in the parent basalt (Fig. 7b; Tab. 2). Two groups of trace elements are further distinguished based on their content relative to the basalt. As in the lower unit, the first group comprises high field strength elements (HFSE) Zr, Ga, Cr, V, Pb, Th, Hf, U and Ta, which are known to be stable during lateritic weathering (Mordberg, 1996), and are thus enriched relatively to their amount in the basalt (Fig. 7b; Fig. 8a-b). The second group comprises depleted elements relative to basalt as Sr, Rb, Ba, Zn, Cu, Ni, Co and As. Enriched trace elements in weathering horizons ($\sum_{HFSE}$) of this litho-section show increasing contents from the mottled clay M1b to the surface pebbly horizon M2b (Tab. 2). In contrast, Nb, Ba, Zn, Ni, Cu, Co, As, Sc, U and Ta contents decrease toward the surface. At the top of mottled clay (M1b), Nb, Zr, Y, Ni, Ga, Cr, V, Sc, Pb, Th, Hf, U and Ta are relatively enriched (Fig. 7b and Tab. 2). In this profile section, trace elements behave differently, except some HFSE (e.g., $r^2_{Hf\text{-}Ga}$= 0.90; Fig. 8a-b). They instead vary with IOL and major elements like Al_2O_3 and TiO_2 (e.g., $r^2_{Ni\text{-}TiO2}$=-0.87; Fig. 8d-e) owing to kaolinite and anatase control, while negative relation to Fe_2O_3 content (e.g., $r^2_{Ni\text{-}Fe2O3}$=-0.63; Fig. 8g-h) is suggestive of their release from Fe-rich primary minerals (olivine, pyroxene) upon still ongoing basalt weathering. The geochemical discrimination diagram Zr/Ti *vs* Nb/Y (Fig. 8i; based on Winchester and Floyd, 1977) further strengthens the parental lithological differences (Figs. 8b-d-f-g). Basalt is richer in Ti, Zr, Nb and Y than granite, and the behaviour of these elements is quite contrasted in the

two weathered litho-sections (Tabs. 1 and 2) that portrays maintained geochemical signatures during sequential profile maturation.

4.3. REE behavior across the composite profile

REE contents vary from 0.13 ppm to 516 ppm in the composite profile (Tab. 3) with maximum abundances for LREE. In the lower section, LREE and HREE are mostly depleted in the nodular horizon M1g while enriched in the yellowish-red mottled clays M2g relative to the granite, except La, Ce and Tb that are depleted in the overall lower unit of the profile (Fig. 9a; Tab. 3). In the upper section, LREE namely La, Pr, Ce and Nd are enriched while Sm, Eu, Gd and LREE show contrasted behavior and are either depleted or enriched relative to the basalt (Fig. 9b; Tab. 3). REE vertical distribution displays a slight increase along the profile section with apparent enrichments at the top of the nodular duricrust M1g and the top of the yellowish mottled clay (Tab. 3).

The C1 chondrite normalized REE spectra (Mc Donough and Sun, 1995) for granite and weathered samples are similar and evidence important HREE fractionation relative to LREE along the lower section of the profile (Fig. 9c). The normalization pattern further highlights Ce* and Eu* anomalies (Fig. 9c; Tab. 3). Indeed, the granite and the yellowish-red mottled clay M2g show Ce/Ce* values of ~1 (Tab. 3) indicating no depletion/enrichment relative to La and Pr (Fig. 9c). Lowest Ce/Ce* values with minimum of 0.41 in the nodular horizon M1g (Tab. 3) further imply negative Ce anomaly in this horizon (Fig. 9c). Normalization patterns also highlight highest Ce/Ce* for the basalts (0.95) while decreasing values in the yellowish mottled clay M1b and the pebbly surface horizon M2b to 0.65 (Tab. 3) are also significant of reducing conditions upon basalt weathering (Fig. 9d).

The C1 chondrite normalized Eu/Eu* further display negative anomalies across the whole profile (Fig. 9c-d). Granite (Eu/Eu*=0.53) and basalt (Eu/Eu*=0.91) anomalies (Tab.

265 3) first indicate a depleted Eu granite relative to Eu- and plagioclase rich basalt. Eu/Eu*
266 variations across the profile further show lower values in the granite section (~0.6) with well-
267 marked anomalies (Fig. 9c), while the basalt litho-section has higher values and lower
268 anomalies in (~0.8; Fig. 9d). Eu/Eu* increases with IOL in the granite section of the profile
269 (Fig. 10a) with no clear trend but higher IOL and Eu/Eu* in the basalt section (see also Tab. 1
270 and Fig. 6). The overall ∑REE dependence on IOL is also better expressed in the lower part
271 of the litho-section on granite ($r^2_{\sum REE\text{-}IOL=}$ 0.96) than in the higher litho-section on basalt (Fig.
272 10b).

273 Highest La/Y values occur in the nodular horizon M1g, while the lowest values are
274 recorded upper in the yellowish-red mottled clay M2g in the lower section; then La/Y
275 decreases upward in the upper section of the profile (Tab. 3). Ratio La/Y evolves like ∑REE
276 in the higher and the lower section of the profile ($r^2_{\sum REE\text{-}La/Y}$ = 0.97 *vs*.0.87), while $(La/Yb)_N$
277 varies less with ∑REE (r^2=0.66; Fig. 10c). The $(Gd/Yb)_N$ ratio show lowest values (2-4) in the
278 nodular horizon, the yellowish red mottled clay and the surface pebbly horizon (Tab. 3). Its
279 highest value 10.33 along with highest $(La/Yb)_N$ in yellowish mottled clays M1b of the upper
280 section on basalt (Fig. 10d) highlight LREE enrichment relative to HREE in early stage of
281 lateritic weathering. Eu/Eu* vs $(Gd/Yb)_N$ differentiates end terms fractionation between the
282 lower litho-section on granite and the upper litho-section on basalt (Fig. 10e), while $(La/Yb)_N$
283 and Ce/Ce* differently evolve (Fig. 10f).

284 In the lower litho-section on granite, ∑REE are highly related to Fe_2O_3 and P_2O_5
285 amounts (r^2=0.97, and r^2=0.95, respectively) indicating iron oxides and phosphates as
286 potential hosts minerals (Braun et al., 1993). Inversely, their opposite behavior from SiO_2 and
287 Al_2O_3 (r^2=-0.94, and r^2= - 0.74, respectively) is indicative of their release during dissolution of
288 primary Si-Al minerals without secondary trapping by kaolinite. However, in the upper
289 section on basalt, ∑REE variations with SiO_2, Al_2O_3, TiO_2, MnO_2 and P_2O_5 (053 < r^2 < 0.99)

290 indicate kaolinite, iron oxides, ilmenite and phosphates as potential carriers. But, their
291 behavior different from FeO_2 (r^2=-0.88) is instead indicative of ongoing REE release from
292 residual ferruginous primary minerals (olivines and pyroxenes) without trapping by secondary
293 iron oxy-hydroxides given the low IOL calculated in the upper section of the profile (see Tab.
294 1; and Fig. 6).
295

296 **5. Discussion**

297 5.1. Differentiated geochemical weathering across the composite lateritic weathering profile

298 Petro-geochemical differentiations across the composite profile reflect different in-situ
299 weathering paths owing to the different lithologies and age of each profile litho-section that
300 control the distribution of major elements. These differentiations resulted in a Si-rich lower
301 section on granite while Fe-rich horizons developped on basalt. The lower litho-section on
302 granite is mainly characterized by processes of kaolinization to weak laterization (see Fig. 6),
303 which have preserved parent rock structure in the uppermost mottled clays horizon, with
304 obvious ferruginizations in maintained fractures (Figs. 4e). Heating effect of basalt
305 outpouring ~ 9 Myr. ago on clay rich mottled clays may have further exaggerated the pre-
306 existing fractures in a “shrinkage slots” pattern, that favored to Fe-oxyhydroxides
307 crystallizations/coating (Fig. 4e), and/or transfers and nodular segregations of iron in the
308 underlying granitic litho-section during late Neogene weathering (Fig. 11). The lowermost
309 nodular horizon M1g of the granite litho-section therefore results from relative downward
310 enrichment of Fe (Figs. 6 and 7a) that partially deleted the original granite structure (see Figs.
311 4b). At the top of this nodular horizon, formation of centimeter sized ferruginous concretions
312 and nodules (Figs. 4c) in a loose inter-nodular matrix along with increasing Fe_2O_3 content and
313 IOL (Fig. 6; Fig. 7a) emphasize mobilization and further segregation of iron under contrasted

conditions in an area of water table fluctuation (see Beauvais, 1999). In such conditions, formation of nodules results from redox-controlled dissolution/precipitation processes of iron, which preferentially accumulated in kaolinite-rich domains of mottled clays (Tardy and Nahon, 1985; Ambrosi and Nahon, 1986a; Muller and Bocquier, 1986; Tardy, 1997; Beauvais, 1999, 2009; Löhr et al., 2013) to ultimately form ferruginous nodules and/or nodular ferricrete.

Trace elements display contrasted behaviors; Cu, Ni, Co are enriched in weathering horizons on granite while depleted in horizons on basalt. Trace elements composition also reveals increasing contents of Nb, Zr, Ga, Ni, Co, Sr, and Rb upward, which vary with major elements in the lower litho-section on granite (Tab. 2). In contrast, these elements decrease from the bottom to the top of the upper litho-section of the profile on basalt (Tab. 2), after their release from relic pyroxene and olivine. Trace elements behavior to major elements ($0.56 \leq r^2 \leq 0.71$) in the basalt litho-section portrays their enrichment in the weathering profiles by trapping in iron oxides, anatase and possibly P-bearing minerals (Ambrosi and Nahon, 1986b; Mordberg, 1996).

Fractionation differences of LREE (La and Ce) vs HREE (Yb) and Ce* anomaly depend on varying redox conditions across the composite profile (Braun et al., 1993; Boulangé and Colin, 1994; see also Brown and Helmke, 2003; Su et al., 2017), e.g., as illustrated in figure 4e. The variation of $(La/Yb)_N$ *vs.* $\sum$REE (Fig. 10c) corroborates differential REE fractionation with laterization grade (different IOL) and possibly pH variations in the two litho-sections (Zarasvandi et al., 2012). Negative Ce/Ce* anomaly is stronger in the granite litho-section than on basalt (Figs. 9b-c) reflecting differences of redox conditions, (Braun et al., 1993; Beauvais, 1999; Momo Nouazi et al, 2019). Ce depletion relative to La and Pr generally depends on reducing conditions (see Compton et al., 2003; Nyakairu and Koeberl, 2001). The Eu/Eu* negative anomaly is also stronger in the granite

339 litho-section than on basalt (Fig. 9c-d) that emphasizes the lithological dependence of less
340 weathered horizons on relatively young basalt compared to granite. Higher Eu/Eu* anomaly
341 rand relatively higher IOL in the basalt litho-section (Fig. 6) depend on residual Fe-Mg
342 minerals in the early-stage weathering but moderate laterization process of basalt (Tab. 1 and
343 Fig. 6).
344 The last stage of profile development after the emplacement of the ~ 9 Myr. old
345 basalts upon weathered granitic regolith was still sustained by per-humid climatic conditions
346 on Adamaoua that also prevailed more widely across the continental intertropical belt during
347 the Mid-Miocene climatic optimum (e.g., Beauvais et al., 2008; Jean et al., 2020).
348
349 **5.2. Landscape erosion signatures from the composite lateritic weathering profile**
350 The unconformity between the weathered basaltic cover and the mottled clay horizon
351 formed in situ on granite (Fig. 3a) marks the erosion surface upon which the basalts outpoured
352 ~ 9 Ma ago. Around Mayo-Bali (Fig. 1), this erosion surface exposes deeper weathering
353 horizons, like mottled clays, after truncation of the top ferricrete (Fig. 11a-b) although
354 remnants may be preserved at lower altitudes (~1200 m) over syn-tectonic granitoids (Fig. 2a-
355 d). The general rolling morphology of the pediplain formed on granite (Fig. 1b) does not
356 show younger stepped relics that suggests slow landscape incision and erosion limited to the
357 duricrusted top of lateritic profiles (see Chardon et al., 2018). Under persistent per-humid
358 climatic conditions, erosion of ferricrete-capped glacis/pediment apparently prevailed over
359 rivers down-cutting (Grandin, 1976). That resulted in a low relief saprolite/mottled clay-
360 mantled erosion surface (Fig. 11b) in between shallow incised valleys, in which Neogene
361 basalts have spilled out covered the downslope eroded portions of the lateritic pediplain
362 previously formed on granite (Fig. 11c).

Mid- to late Miocene volcanics outpourings through pre-existing structurally controlled discontinuities across the granitic basement resulted in limited local incision of previous lateritic pediplains formed on granites. Note also that iron-poor Pan-African basement of Adamaoua limited regolith duricrusting and strength allowing lateritic profiles truncation on pediplains. After ~ 9 Ma, basalts/andesites weathered and their lateritic regolith evolved with marked hillside incisions into a younger surface (Figs. 1b and 2e-f). Late morphogenetic processes related to weathering/duricrusting on basalts also included late Neogene lateritic weathering previously formed profiles on the granitic basement (Fig. 11d). Landscape topography has been only locally rejuvenated under persistent per-humid climatic conditions and sustained drainage that have however mostly enhanced weathering and geochemical differentiations in the composite profile (Fig. 11d). In Eastern Adamaoua, rugged erosional terrains with average slope gradient of ~4 to 5 % between wide domains of pediplains (Fig. 1b) also portray hillslope erosion that preferentially occurred on inherited litho-structural discontinuities (see also Sawadogo et al., 2020). Landscape physical rejuvenation was also previously observed in western highlands of Cameroon (Momo Nouazi et al., 2019) on Mid-Miocene basalts and trachytes, and possibly occurred during a period (i.e., Pliocene) of mechanical (clastic) erosion (Tchouatcha et al., 2010).

6. Conclusion

Upon Eastern Adamoua highland, Neogene basalts outpourings through inherited structural discontinuities have locally spread in shallow incisions of low-relief lateritic pediplains previously established upon granitic basement. This resulted in the formation of superimposed composite weathering profiles on granite and basalt. Though the studied profile is moderately lateritised, the two sections on granite and basalt are differentiated by their variable index of laterization (IOL), and specific behaviors of some trace and REE elements

388 relative to their respective amounts in each parent rock. Transition elements Cu, Ni and Co
389 are more enriched in the weathering section on granite than on basalt. Owing to contrasted
390 amounts of heavy minerals in the two parent rocks, Zr, Ti, Nb and Y also shows a contrasted
391 pattern, with decreasing (Zr/Ti) and increasing (Nb/Y) in the granite litho-section while
392 (Zr/Ti) remains constant in basalt litho-section. Differences of silicate minerals composition
393 of the two parent rocks also induced a differential weathering with negative Eu* anomaly
394 higher on granite section than on basalt. Eu* also increases with increasing IOL in the granite
395 litho-section, while REE further fractionated as indicated by the amplitude of co-variations of
396 $(La/Yb)_N$ and Ce*. After Neogene basalt outpourings on pediplain landscapes of Adamaoua
397 highland, persistent humid climatic conditions and efficient drainage have sustained rock
398 weathering processes with a noticeable differentiation and fractionation of trace and REE
399 elements across the composite lateritic profile.
400
401 Acknowledgements- The IRD program JEAI is thanked for funding and support to the
402 MORPHOCAM project under which this work has been done. Financial support of the APIC
403 annual programs (2019-2020) from the “Centre de Recherche et d’Enseignement des
404 Géosciences de l’Environnement” (CEREGE) is also acknowledged. IRD (Disco department)
405 is also thanked for granting MNM stays at Cerege, Aix Marseille Université, OSU Pytheas,
406 France. Remarks and suggestions from two anonymous reviewers and the editor Dr.
407 Scarciglia are also much acknowledged.
408
409
410

411 **References**

412 Allix, P. Legoux, O., Robert, P., 1984. Essai d'interprétation géodynamique de l'évolution
413 Mésozoïque des sous-bassins du fossé de la Bénoué. Bull. Soc. Géol., France (7), 26,
414 1061-1068.

415 Ambrosi, J-P., Nahon, D., 1986a**.** The epigenetic replacement of kaolinite by hematite in
416 laterite- petrographic evidence and the mechanisms involved. Geoderma 37(4), 283-294.

417 Ambrosi, J-P., Nahon, D., 1986b. Petrological and geochemical differentiation of lateritic iron
418 crust profiles. Chemical Geology 57, 371-393.

419 Babechuk, M.G., Widdowson, M., Kamber, B.S., 2014. Quantifying chemical intensity and
420 trace element release from two contrasting profiles, Decan Traps, India. Chemical
421 geology 365, 56-75.

422 Beauvais, A., 1999. Geochemical balance of laterization processes and climatic signaturs in
423 weathering profiles overlain by ferricretes in Central Africa. Geochimica et
424 Cosmochimica Acta 63 (1999), 3939-3957.

425 Beauvais, A., 2009. Ferricrete biochemical degradation on the rainforest savannas boundary
426 of Central African Republic. Geoderma 150, 379-388.

427 Beauvais, A., Bonnet, N.J., Chardon, D., Arnaud, N., Jayananda, M., 2016. Very long-term
428 stability of passive margin escarpment constrained by 40 Ar/ 39 Ar dating of K-Mn
429 oxides. Geology 44, 299-302. https://doi.org/10.1130/G37303.1

430 Beauvais, A., Chardon, D., 2013. Modes, tempo, and spatial variability of Cenozoic cratonic
431 denudation: The West African example. Geochem. Geophys. Geosyst. 5(5), 1590-1608.
432 doi:10.1002/ggge.20093.

433 Beauvais, A., Ruffet, G., Hénocque, O., Colin, F., 2008. Chemical and physical erosion
434 rhythms of the West African Cenozoic morphogenesis: The 39Ar-40Ar dating of

435 supergene K-Mn oxides. Journal of geophysical research. Earth surface 113, F04007,
436 doi:10.1029/2008JF000996.

437 Boulangé, B., Colin, F., 1994. Rare-earth element mobility during conversion of nepheline
438 syenite into lateritic bauxite at Passa Quatro, Minais Gerais, Brazil. Appl.Geochem. 9,
439 701-711.

440 Braun, J.J., Pagel, M., Herbillon, A., Rosin, C., 1993. Mobilization and redistribution of REEs
441 and thorium in syenitic lateritic profile: A mass balance study. Geochim. Cosmochim.
442 Acta 57, 4419-4434.

443 Brown, D.J., Helmke, P.A., 2003. Robust geochemical indices for redox and weathering on a
444 granitic laterite landscape in Central Uganda. Geochim. Cosmochim. Acta 67(15), 2711-
445 2723.

446 Burke, K., 2001. Origin of the Cameroon line of volcano-capped swells. The Journal of
447 Geology 109, 349-362.

448 Burke, K., Gunnell, Y., 2008. The African erosion surface: a continental-scale synthesis of
449 geomorphology, tectonics, and environmental change over the past 180 million years.
450 Geological Society of America, Memoir 201 1 - 66.

451 Chardon, D., Grimaud, J.L., Beauvais, A., Bamba, O., 2018. West African lateritic pediments:
452 Landform-regolith evolution processes and mineral exploration pitfalls. Earth science
453 review 179, 124-146.

454 Chardon, D., Grimaud, J-L., Rouby, D., Beauvais, A., Christophoul, F., 2016. Stabilization of
455 large drainage basins over geological timescales: Cenozoic West Africa, hot spot swell
456 growth and the Niger River. Geochem. Geophys. Geosyst. 17, (3), 1164-1181.

457 Colin, F., A., Beauvais, G., Ruffet, Hénocque, O., 2005. First 40Ar/39Ar geochronology of
458 lateritic manganiferous pisolites: Implications for the Palaeogene history of a West
459 African landscape. Earth Planet Science Letter, 238, 172-188.

460 Compton, S.J., White, A.R., Smith, M., 2003. Rare earth element behavior in soils and salt
461 pan sediments of a semi-arid granitic terrain in the Western Cape, South Africa.
462 Chemical geology 201, 239-255.

463 Delor, C., Bernard, J., Tucker, R.D., Roig, J-Y., Bouyo Houketchang, M., Coueffe, R., Blein,
464 O., 2021. 1/1000000-scale geologic map of Cameroon. Second edition.

465 Deruelle, B., Moreau, C., Nkoumbou, C., Kambou, R., Lissom, J., Njonfang, E., Ghogomu,
466 T.R., Nono, A., 1991. The Cameroon Line: a review. In: Kampunzu, A.B., Lubala, R.T.
467 (Eds.), Magmatism in Extensional Structural Settings, The Phanerozoic African Plate.
468 Springer-Verlag, Berlin, pp. 274-327.

469 Fosso, J., Ménard, J.-J., Bardintzeff, J.-M., Wandji, P., Tchoua, F. M., Bellon, H., 2005.
470 Lavas from the Mount Bangou area: A first Eocene volcanic episode with transitional
471 affinities of Cameroon Line. C. R. Géoscience 337(3), 315-325.

472 Ganwa, A.A., Wolfgang, S., Wolfgang, F., Shang, C.K., 2011. Geochemistry of magmatic
473 rocks and time constraints on deformational phases and shear zone slip in the Méiganga
474 area, central Cameroon. International Geology Review, 53: 7, 759-784. doi:
475 10.1080/00206810903211161

476 Girod, M., Dautria, J.M., Bali, E., Soba, D., 1984. Pétrologie-Estimation de la profondeur du
477 Moho sous le massif volcanique de I'Adamaoua (Cameroun), à partir de l'étude des
478 enclaves de lherzolite. Compte rendu de l'Académie des Sciences, Paris, 298, 2, 699-704.

479 Grandin, G., 1976. Aplanissements cuirassés et enrichissement des gisements de manganèse
480 dans quelques régions d'Afrique de l'Ouest. Mémoires de l'ORSTOM 82, 1-276.

481 Grimaud, J.-L., Chardon, D., Beauvais, A., 2014. Very long-term incision dynamics of big
482 rivers. Earth. Planet. Sci. letters 405, 74-84.

483 Jean, A., Beauvais, A., Chardon, D., Arnaud, N., Jayananda, M., Mathe, P.E., 2020.
484 Weathering history and landscape evolution of Western Ghats (India) from 40Ar/39Ar
485 dating of supergene K–Mn oxides. Journal of the Geological Society 177, 523-536.
486 https://doi.org/10.1144/jgs2019-048

487 Kagou Ndongmo, A., Nkouathio, D.G., Pouclet, A., Bardintzeff, J-M., Wandji, P., Nono, A.,
488 Guillou, H., 2010. The discovery of Late Quaternary basalt on Mount Bambouto:
489 implications for recent widespread volcanic activity in the southern Cameroon Line.
490 Journal of African Earth Sciences 57, 96-108.

491 Lasserre, M., 1961. Etude géologique de la partie orientale de I'Adamaoua (Cameroun
492 central). Territoire Camerounais. Bullettin de la Direction des mines et de la Géologie 4,
493 130 p, carte 1/500000.

494 Löhr, S.C., Grigorescu, M., Cox M.E., 2013. Iron nodules in ferric soils of the Fraser Coast,
495 Australia: relicts of laterisation or features of contemporary weathering and pedogenesis?
496 Soil Research 51, 77-93. http://dx.doi.org/10.1071/SR12372

497 Marzoli, A., Piccirillo, E.M., Renne, P.R., Bellieni, G., Iacumin, M., Nyobe, J.B., Tongwa,
498 A.T., 2000. The Cameroon Volcanic Line revisited: Petrogenesis of continental basaltic
499 magmas from lithospheric and asthenospheric mantle sources. Journal of Petrology 41,
500 pp. 87-109.

501 Marzoli, A., Renne, P. R., Piccirillo, E. M., Francesca, C., Bellieni, G., Mel, A. J., Nyobe, J.
502 B., N'ni, J., 1999. Silicic magmas from the continental Cameroon Volcanic Line (Oku,
503 Bambouto and Ngaoundéré): 40Ar/39Ar dates, petrology, Sr-Nd-O isotopes and their
504 petrogenetic significance. Contribution Mineral Petrology 135, 133-150

505 Mc Donough, W.F., Sun, S.S., 1995. The composition of the Earth. Chemical geology 120,
506 223253.

507 Momo Nouazi, M., Beauvais, A., Tematio, P., Yemefack, M., 2019. Differentiated Neogene
508 bauxitization of volcanic rocks (western Cameroon): Morpho-geological constraints on
509 chemical erosion. Catena 194, 104685.

510 Mordberg, L.E., 1996. Geochemistry of trace elements in Paleozoic bauxite profiles in
511 northern Russia. Journal of geochemical exploration 57, 187-199.

512 Muller, J-P., Bocquier, G., 1986. Dissolution of kaolinites and accumulation of iron oxides in
513 lateritic-ferruginous nodules: Mineralogical and microstructural transformations.
514 Geoderma 37(2), 113-136.

515 Nahon, D., 1991. Introduction to the petrology of soils and chemical weathering. A Wiley-
516 Interscience Publication, 313 p.

517 Nguetnkam, J-P., Solleiro-Rebolledo, E., Díaz-Ortegab, J., Tematio, P., 2020. Evaluating
518 weathering of palaeosols in Cameroon (Central Africa) as a tool for paleoenvironmental
519 reconstruction. Catena 194, 104688. https://doi.org/10.1016/j.catena.2020.104688

520 Nyakairu, G.W.A., Koeberl, C., 2001. Mineralogical and chemical composition and
521 distribution of rare earth elements in clay-rich sediments from central Uganda.
522 Geochemical journal 35,13-28.

523 Sawadogo, B., Bamba, O., Chardon, D., 2020. Landform-regolith mapping in the West
524 African context. Ore Geology Reviews 103782.

525 Schellmann, W., 1994. Geochemical differentiation in laterite and bauxite formation. Catena
526 21, 131-143.

527 Su, N., Yang, S., Guo, Y., Yue, W., Wang, X., Yin, P., Huang, X., 2017. Revisit of rare earth
528 element fractionation during chemical weathering and river sediment transport. Geochem.
529 Geophys. Geosyst. 18, 935-955. Doi:10.1002/2016GC006659.

530 Tardy, Y., 1997. Petrology of Laterites and Tropical Soils. Balkema, Rotterdam, 408 p.

531 Tardy, Y., Nahon, D., 1985. Geochemistry of laterites, stability of Al-goethite, Al-hematite,
532 and $Fe3^{+}$-kaolinite in bauxites and ferricretes: an approach to the mechanism of
533 concretion formation. American Journal of Science 285, 865-903.

534 Tardy Y., Roquin C., 1998. Dérive des continents, paléoclimats et altérations tropicales.
535 Editions BRGM, Orléans, 473 p.

536 Tchouatcha, S.M., Njiké Ngaha P.R., Magdy Salah, M., Amr Said, D., Ekodeck, G.E., 2010.
537 Existence of late continental deposits in the Mbere and Djerem sedimentary basins (North
538 Cameroon): Palynologic and stratigraphic evidence. Journal of Geology and Mining
539 Research Vol. 2(6), 159-169.

540 Thomas M. F., 1994. Tropical geomorphology in the tropics. A study of weathering and
541 denudation in low latitudes. John Wiley & Sons, 460 p.

542 Vasconcelos, P., Carmo, I.O., 2018. Calibration denudation chronology through 40Ar/39Ar
543 weathering chronology. Earth Science Reviews, S0012-8252(17)30632-3,
544 doi:10.1016/j.earscirev.2018.01.003

545 Winchester, J.A., Floyd, P.A., 1977. Geochemical Discrimination of Different Magma Series
546 and Their Differentiation Product Using Immobile Elements. Chemical Geology 20, 325-
547 343.

548 Zarasvandi, A., Carranza, E.J.M., Ellahi, S.S., 2012. Geological, geochemical and
549 mineralogical characteristics of the Deh-Now bauxite deposits, Zagros fold belt, Iran. Ore
550 geological review 48, 125-138.

551

552 **FIGURE CAPTIONS**

553 Figure. 1. a) Localization and geologic map of the study area. Structural, petrographic and
554 chronological data are adapted from Lasserre (1961); b) Geomorphological cross
555 section showing regolith landform distribution according to lithological variations in
556 Mayo-Bali area.

557 Figure. 2. Field illustration of lateritic landscape and regolith in the Eastern Adamaoua
558 plateau. a) Late Miocene volcanics morphology surrounded by alluvial plains and
559 granite-related pediments; b) Regolith structure of pediment with a nodular ferricrete
560 embedding massive and undifferentiated fragments; c) Footslope pediment below
561 erosional slope exposing bedrock (black arrow). d) Regolith structure of a footslope
562 pediment; e) Slope erosion of duricrusted lateritic regolith surface formed on basalt;
563 f) Regolith landscape on basalt with hillslope incision and formation of a younger
564 surface.

565 Figure. 3. a) Profile structure of the composite lateritic profile; b-d) Details of horizons
566 showing textural and lithological changes. The blue dotted line marks the lithological
567 unconformity between the lower and the upper part of the profile. b) transition
568 between the nodular horizon M1g and the overlying yellowish-red mottled clay M2g,
569 marked by the yellow dotted line in 3a; c) transition between the mottled clay M2g of
570 the lower section and the yellowish mottled clay M1b of the upper section; d)
571 transition between the yellowish mottled clay M1b and the surface gravelly horizon
572 M2b; evidences of prismatic basalts are shown. Numbered white squares are the
573 collected samples and correspond to samples ID in the tables.

574 Figure. 4. a) Granite sample of the Pan-African basement; b) lower part of the nodular
575 horizon with few nodules; c) Nodular horizon M1g with numerous nodules; d)
576 Undifferentiated structure of mottled clay M2g; e) Mottled clay M2g with preserved
577 granite strcutures.

578 Figure. 5. a) Aphiric basalt sample belonging to the early volcanics on the Adamaoua plateau.
579 b) Mottled clays M1b; c) Surface pebbly horizon M2b.

580 Figure. 6. Composition diagram Al-Si-Fe and index of laterization (IOL) along the composite
581 profile

582 Figure. 7. Granite and basalt normalized trace elements spider-diagrams of the different
583 horizons of the composite profile

584 Figure 8. Trace and major elements scattergrams. a) Hf vs Ga; b) Cr vs Th; c) IOL vs Cr; d)
585 IOL vs Th; e) TiO_2 vs Ni; f) Al_2O_3 vs Ni; g) Fe_2O_3 vs Ni; h) Fe_2O_3 vs Ga; i) Zr/Ti vs
586 Nb/Y

587 Figure. 9. a & b) Granite and basalt normalized REE spider-diagram of the different horizons
588 of the profile. c & d) Chondrite normalized REE spider-diagram of the different
589 horizons of the profile

590 Figure. 10. Geochemical diagrams of REE fractionation across the composite profile. a)
591 Eu/Eu* vs. IOL; b) ∑REE vs. IOL; c) ∑REE vs $(La/Yb)_N$; d) $(La/YB)_N$ vs $(Gd/Yb)_N$;
592 e) Eu/Eu* vs $(Gd/Yb)_N$; f) $(La/YB)_N$ vs. Ce/Ce*

593 Figure. 11. Schematic evolution of the lateritic weathering, and erosion of Eastern Adamaoua
594 landscape. a) Lateritic weathering profile of pediplains formed on the granitic
595 basement of Adamaoua highland. b) Erosion-truncated profile exposing mottled
596 clays at relatively high altitude (> 1200 m a.s.l.) at Mayo-Bali. c) Basaltic strata over

previously truncated profiles of pediplain formed on granite. d) Second stage of landscape dynamics marked by lateritic weathering of both basalt and underlying profile on granite.

TABLES CAPTION

Table 1. Major elements content (wt%) of each sample collected in the composite profile and the fresh rocks. LOI = Lost of ignition; Detection limits: 0.01; (-) = Elements below detection limits; IOL (%) = Index of Laterization; See figure 3a for the location of each sample. Depths of fresh rocks samples are unknown.

Table 2. Trace elements content (µg/g) of each sample collected in the composite profile and the fresh rocks. d.l. = Detection limits; (-) = Elements below detection limits.

Table 3. Rare earth elements content (µg/g) of each sample collected in the composite profile and the fresh rocks. d.l. = Detection limit.

$Ce/Ce^{*}(Ce_{sample}/Ce_{chondrite})/(La_{sample}/La_{chondrite})^{1/2}\ (Pr_{sample}/Pr_{chondrite})^{1/2}$

$Eu/Eu^{*} = (Eu_{sample}/Eu_{chondrite})/(Sm_{sample}/Sm_{chondrite})^{1/2}\ (Gd_{sample}/Gd_{chondrite})^{1/2}$

$(La/Yb)_{N} =(La_{sample}/La_{chondrite})/(Yb_{sample}/Yb_{chondrite})$

$(Gd/Yb)_{N} =(Gd_{sample}/Gd_{chondrite})/(Yb_{sample}/Yb_{chondrite})$.

Figure - Upload high quality Images

Click here to access/download;Figure - Upload high quality Images;Figure. 1.eps

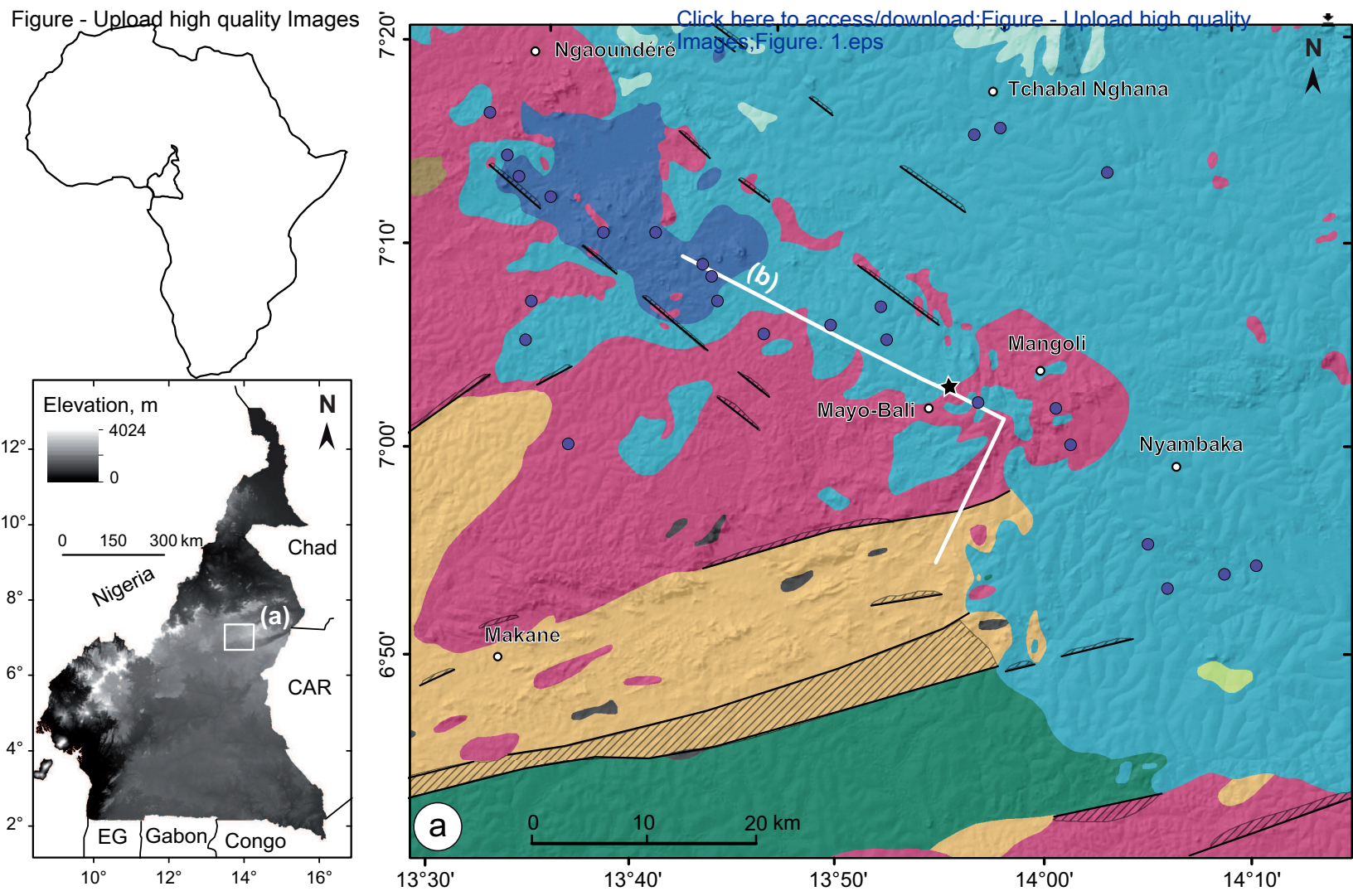

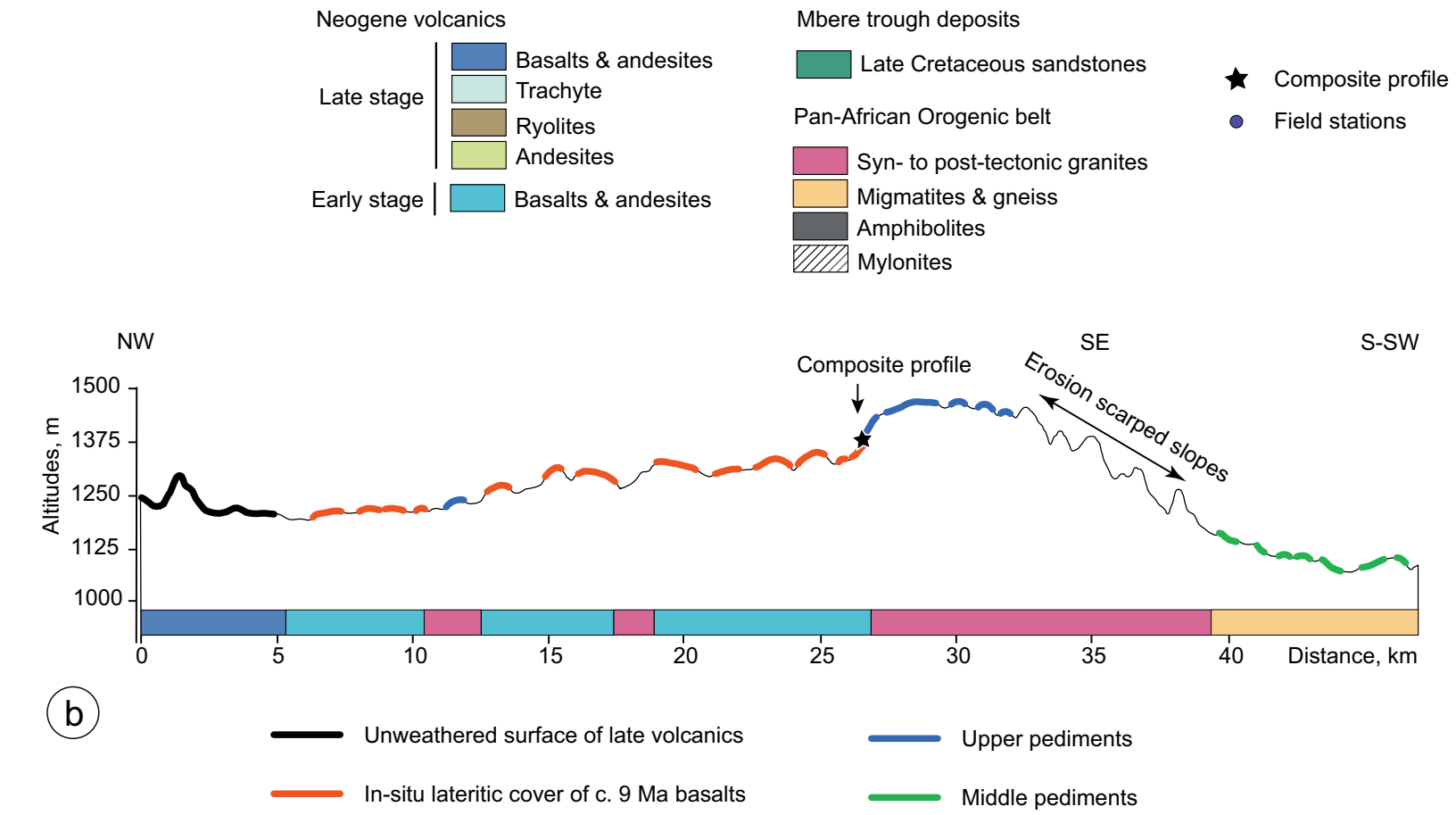

Fig. 1

Fig. 2

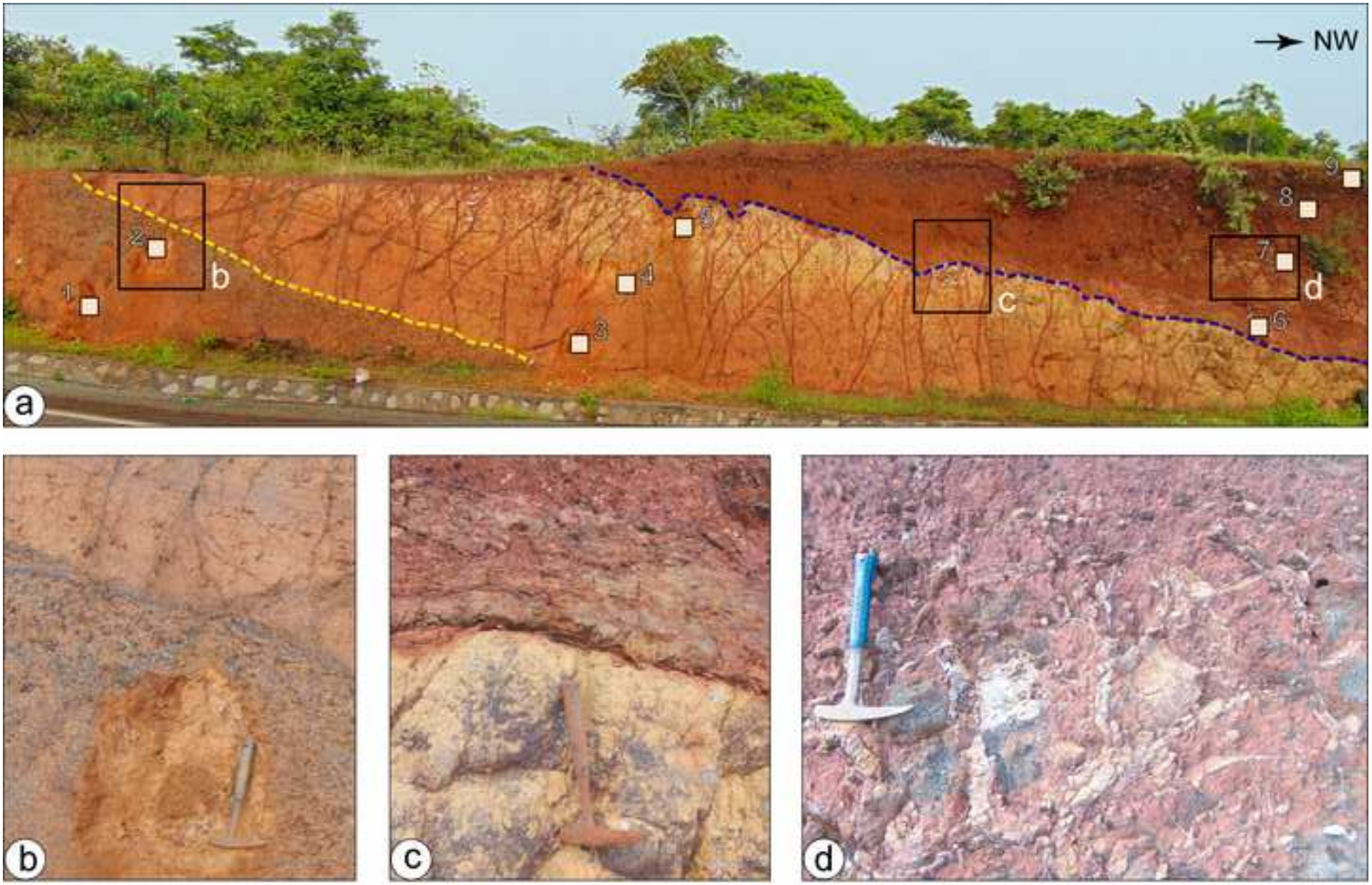

Fig. 3

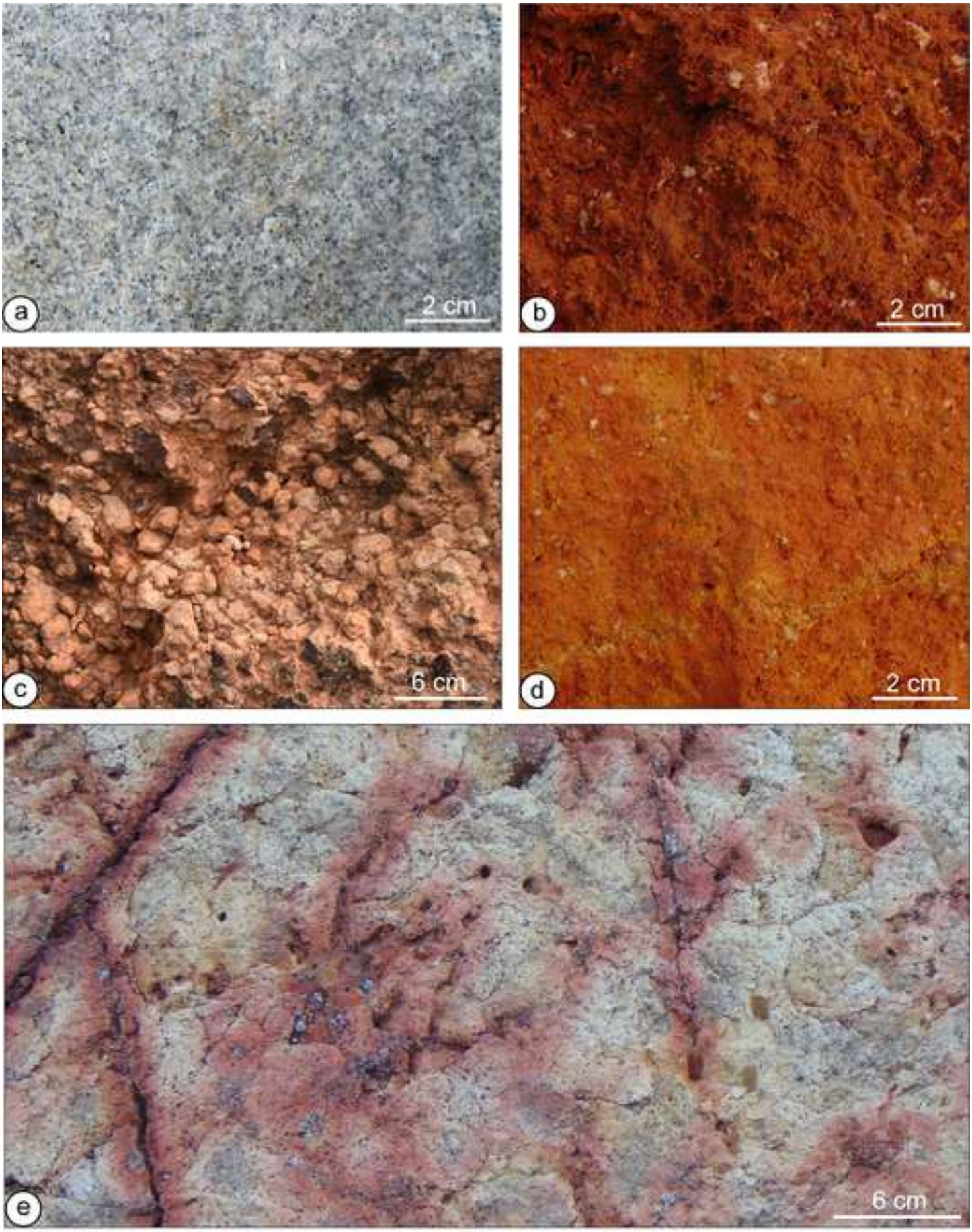

Fig. 4

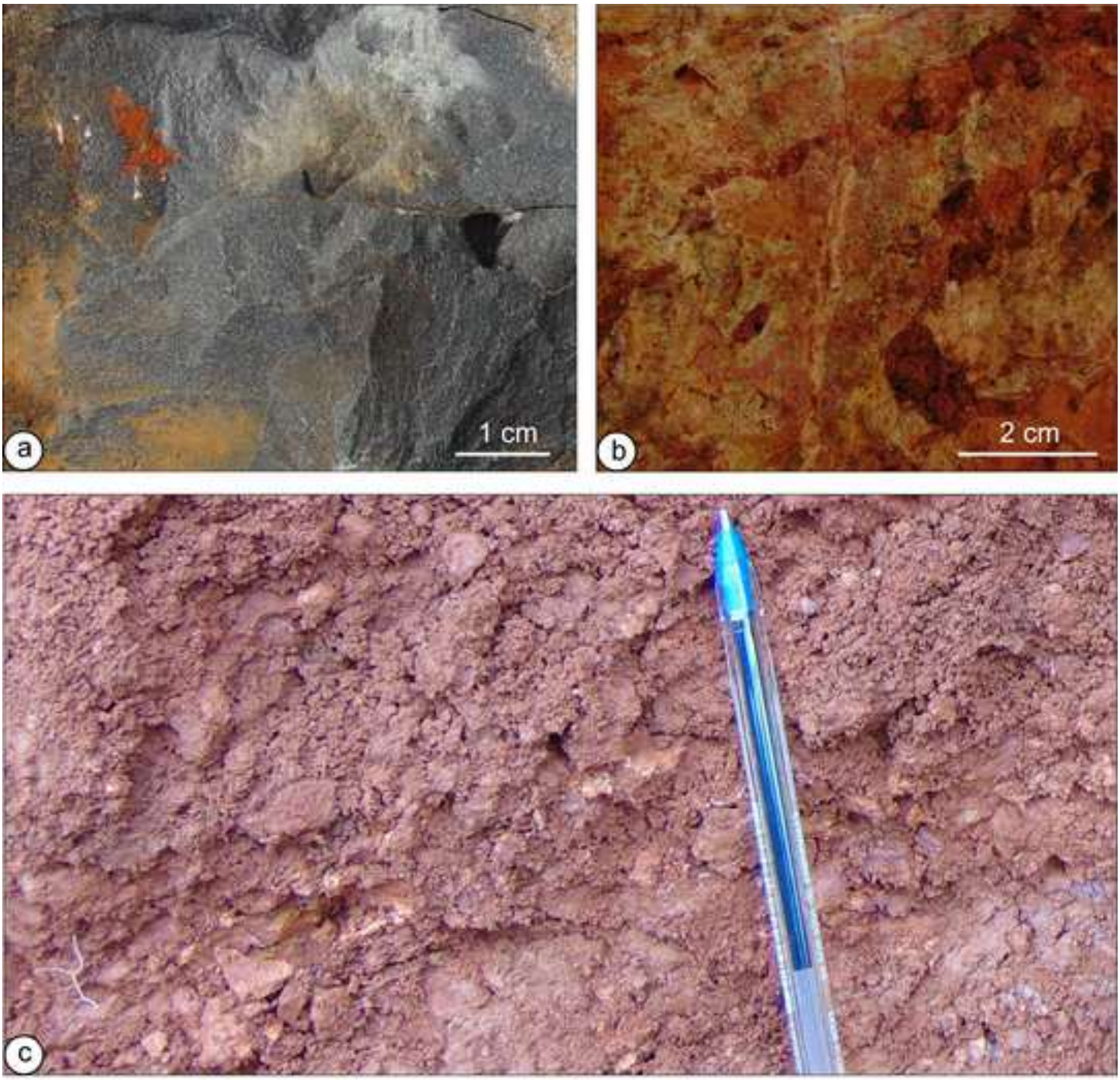

Fig. 5

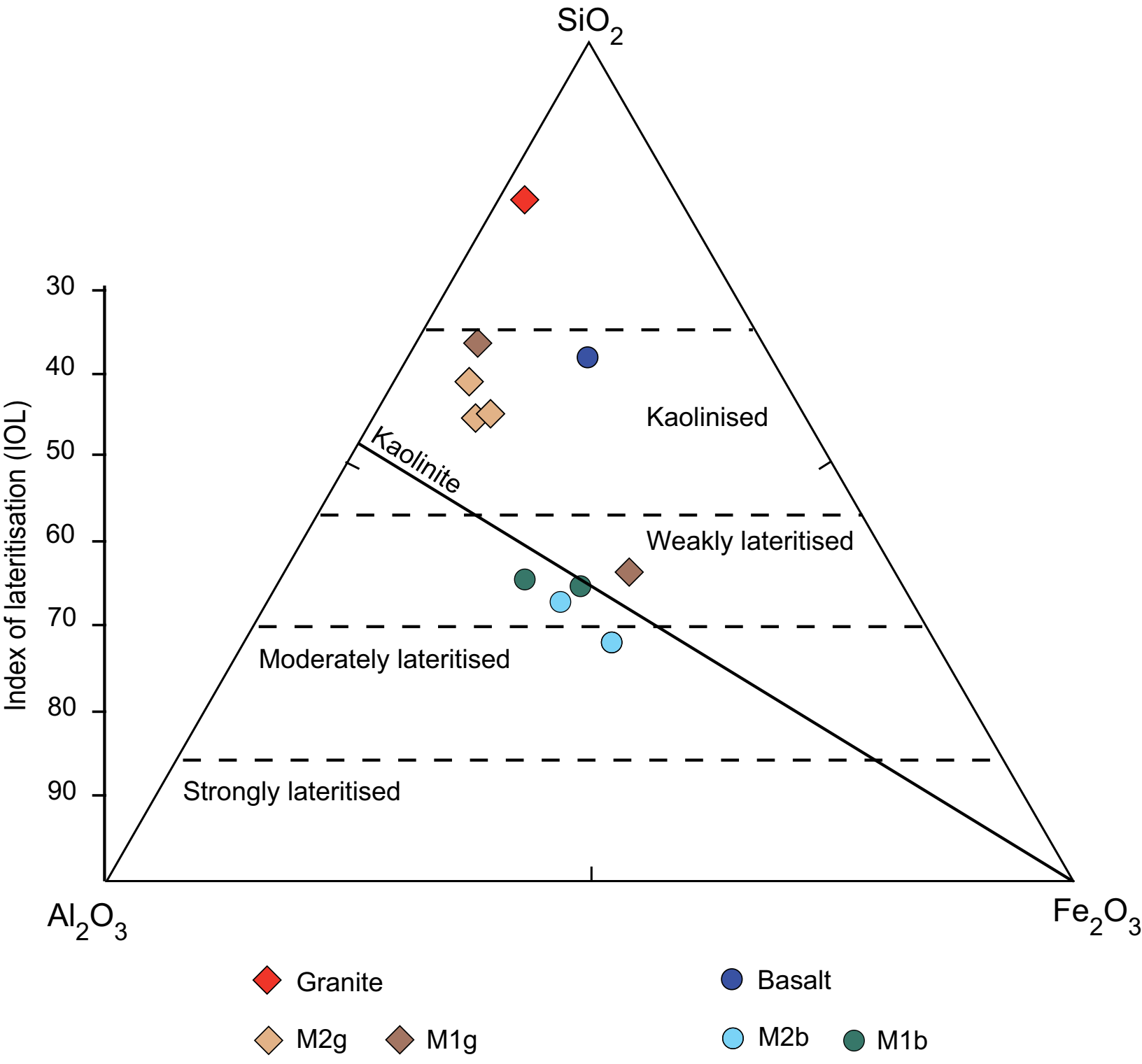

Fig. 6

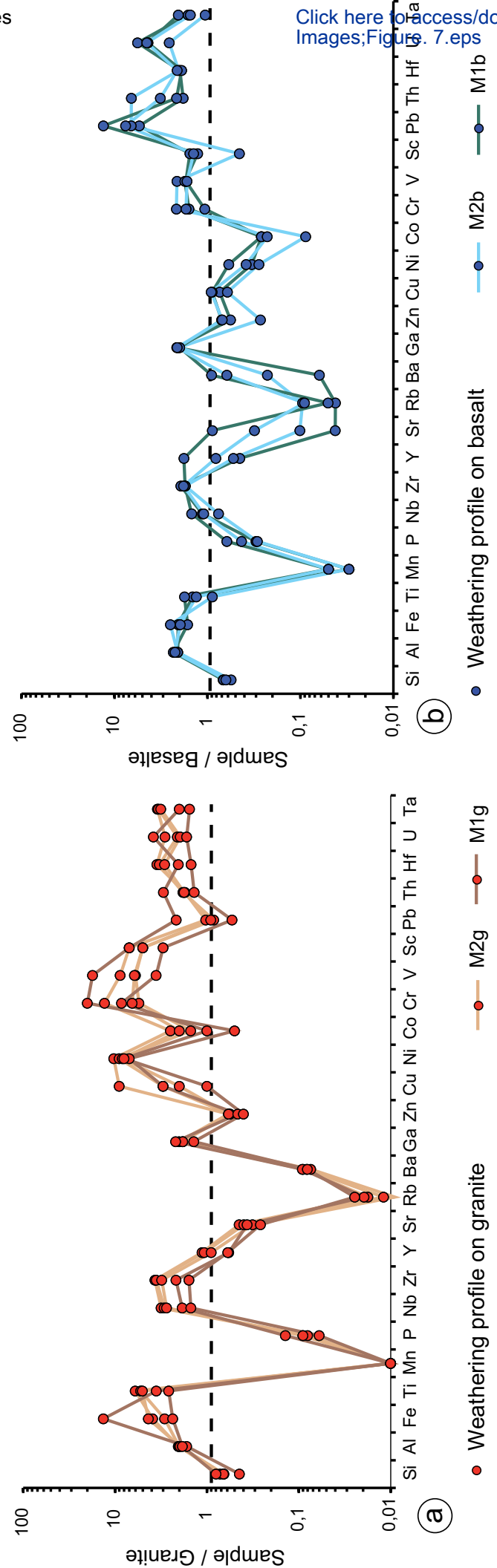

Fig. 7

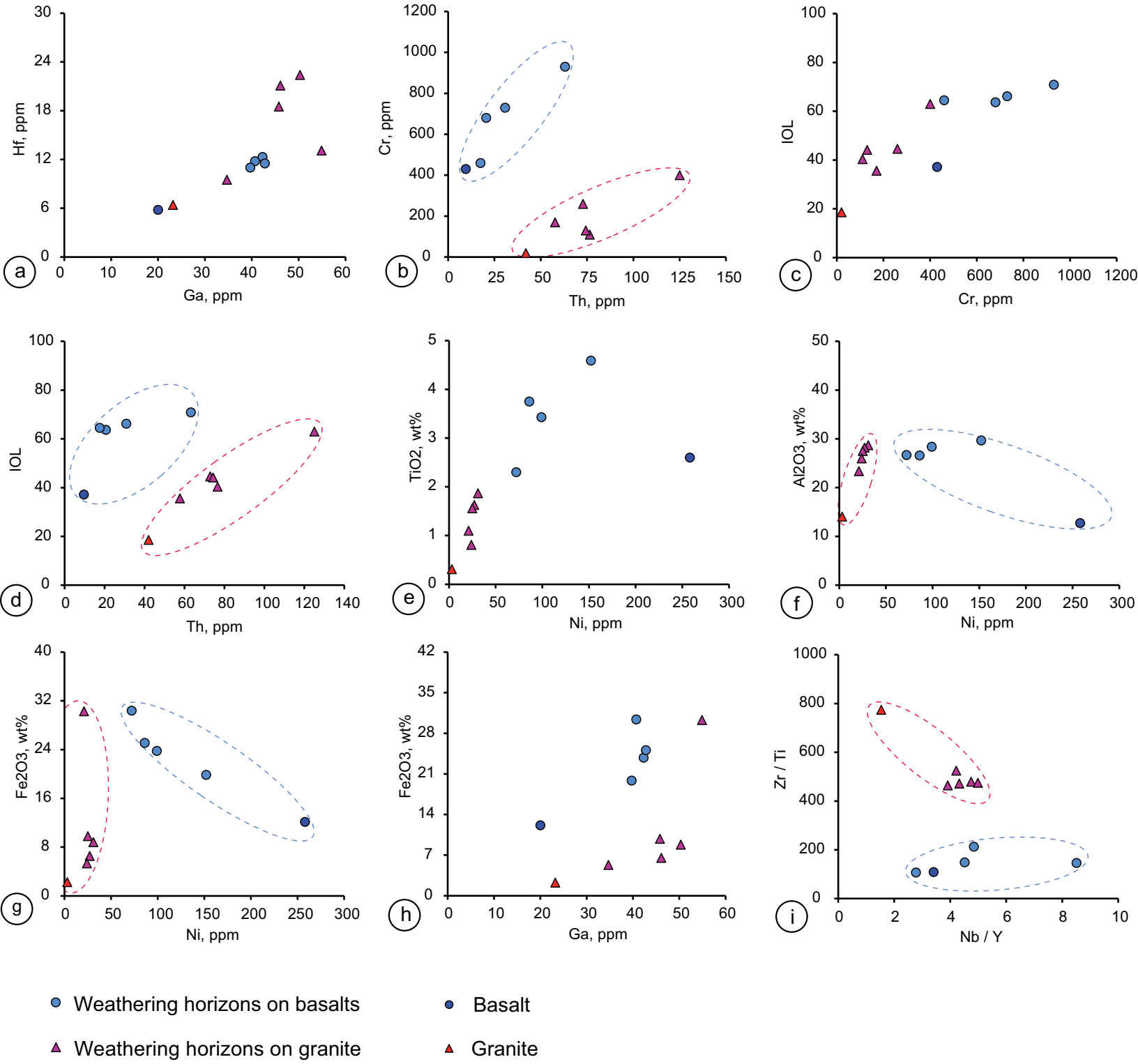

Fig. 8

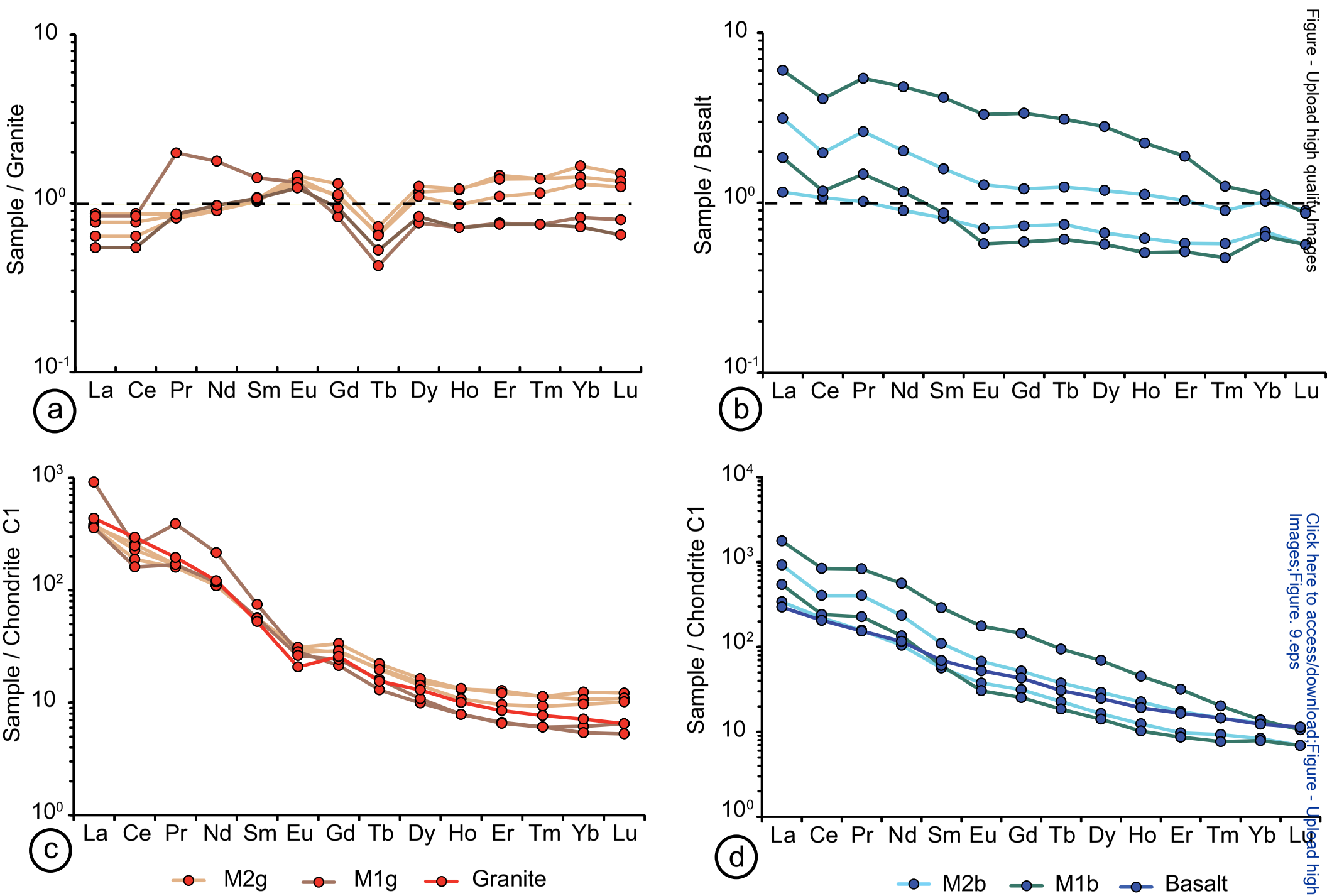

Fig. 9

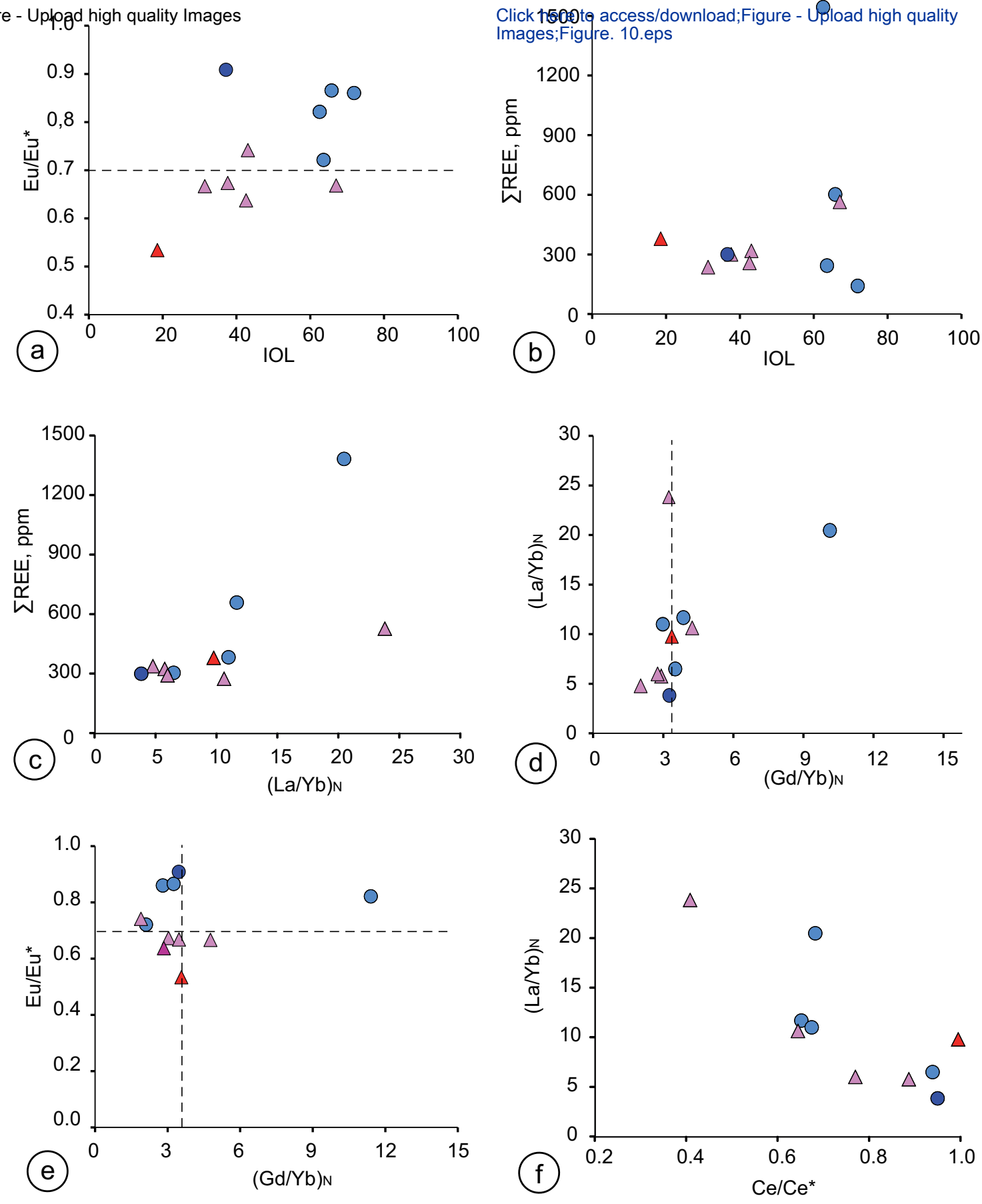

Fig. 10

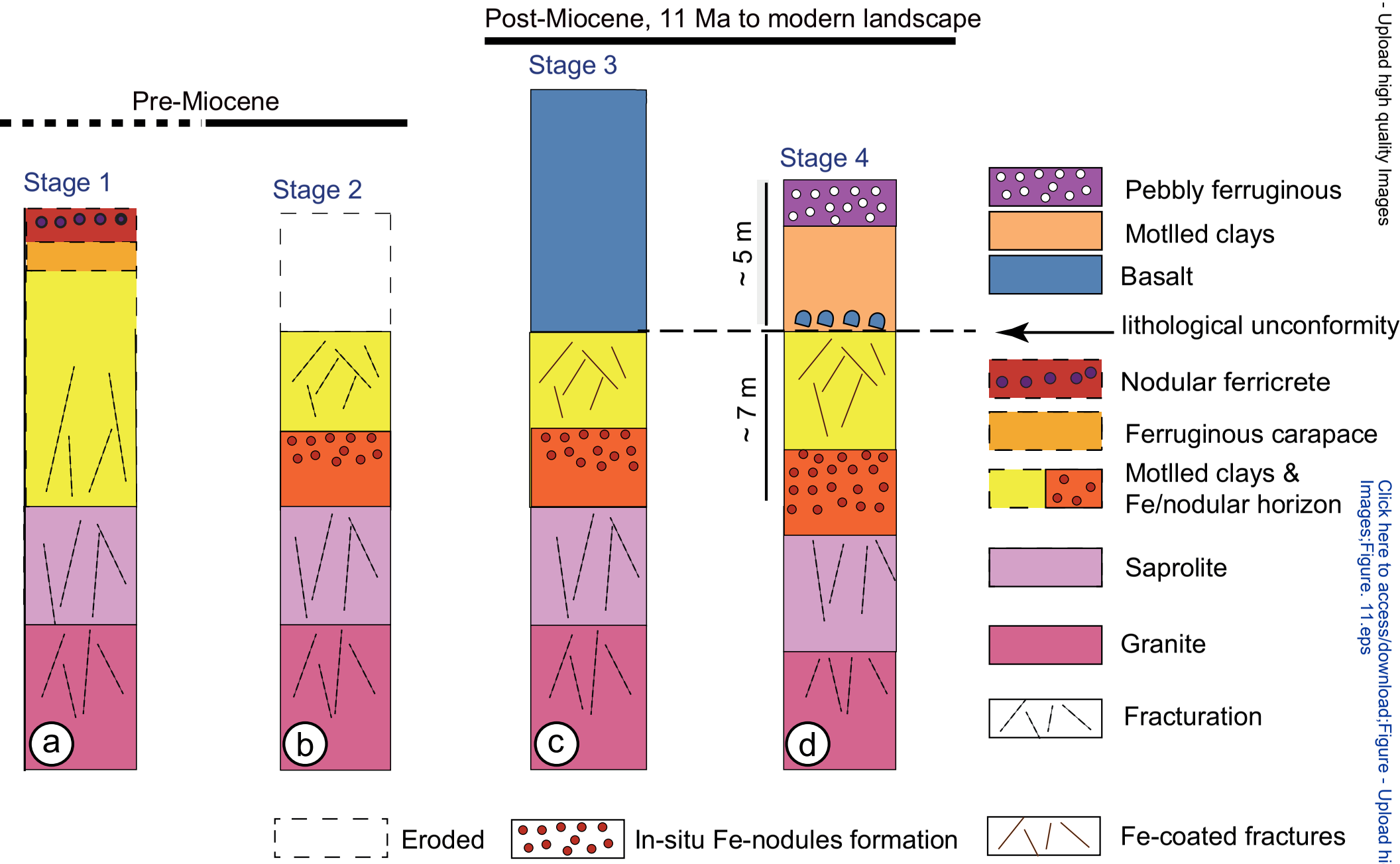

Fig. 11

Table 1

Samples ID	Horizon ID	SiO_2	Al_2O_3	Fe_2O_3	TiO_2	CaO	MgO	Na_2O	K_2O	MnO	P_2O_5	Total	LOI	IOL
MEI-9	M2b	23.5	26.7	30.4	2.3	0.02	0.11	0.01	0.06	0.03	0.29	100.42	11.30	70.8
MEI-8	M2b	26.7	28.4	23.8	3.43	0.03	0.16	0.01	0.06	0.05	0.43	99.9	13.10	66.2
MEI-7	M1b	28.3	29.7	19.85	4.59	0.06	0.14	0.01	0.02	0.05	0.62	99.26	12.60	63.6
MEI-6	M1b	28.5	26.6	25.1	3.75	0.01	0.15	0.01	0.03	0.03	0.3	99.6	12.35	64.5
BAS-MEI		42.1	12.7	12.15	2.6	10.75	11.7	2.61	1.59	0.19	0.95	99.54	1.9	37.2
MEI-5	M2g	46.7	28.7	8.82	1.87	0.02	0.04	0.01	0.05	0.01	0.09	99.56	13.20	44.5
MEI-4	M2g	51.4	28.2	6.54	1.63	0.01	0.03	0.01	0.04	0.01	0.08	100.34	15.05	40.3
MEI-3	M2g	47.2	27.5	9.81	1.56	0.12	0.03	-	0.02	0.01	0.09	98.97	15.65	44.1
MEI-2	M1g	31.6	23.4	30.3	1.1	0.02	0.03	-	0.06	0.01	0.14	99.83	16.65	63.0
MEI-1	M1g	56.8	26.0	5.33	0.81	0.01	0.03	0.01	0.08	0.01	0.06	100.47	16.85	35.5
GRA-MEI		71.5	14.05	2.26	0.31	1.32	0.44	3.38	5.43	0.04	0.08	99.88	0.93	18.6

Table 2

		Nb	Zr	Y	Sr	Rb	Ba	Ga	Zn	Cu	Ni	Co	Cr	V	As	Sc	Pb	Th	Hf	U	Ta
Samples	Horizon ID	dl: 0.1	2	0.1	0.1	0.2	0.5	0.1	2	1	1	1	10	5	5	1	2	0.05	0.1	0.05	0.1
MEI-9	M2b	68.8	489	14.2	93.6	4.5	162	40.7	29	28	72	5	930	460	18	10	33	63.1	11.8	6.45	3.8
MEI-8	M2b	99.4	509	22	288	4.3	443	42.3	75	42	99	13	730	359	6	31	38	30.8	12.3	11.2	5.5
MEI-7	M1b	134	491	48.3	817	2.4	645	39.7	76	41	152	15	680	377	-	28	66	20.6	11	10.9	7.4
MEI-6	M1b	103	546	12.1	38.9	2	44.7	42.8	61	34	86	15	460	369	8	34	27	17.5	11.5	14.1	5.8
BAS-MEI		90.6	282	26.6	923	47.5	715	20	108	46	258	57	430	216	-	22	5	9.58	5.8	2.47	3.6
MEI-5	M2g	68.3	882	15.8	92.7	4.9	93	50.3	29	9	31	5	260	185	5	14	33	72.8	22.4	9.43	3.8
MEI-4	M2g	63.2	855	15	82.6	3.3	84.9	46.1	28	3	27	3	110	126	-	10	27	76.5	21.1	6.91	3.7
MEI-3	M2g	59.8	747	12.6	66.4	2.5	76.7	45.8	29	2	25	4	130	129	-	10	29	74.3	18.5	6.43	3.5
MEI-2	M1g	40.4	522	8.1	75.8	5.4	94.7	54.9	23	3	21	1	400	370	14	14	69	125	13.1	12.6	2.2
MEI-1	M1g	32.5	376	8.3	54.4	6.8	83.5	34.7	20	1	24	2	170	75	-	6	17	57.7	9.5	5.48	1.7
GRA-MEI		21.7	240	14.1	208	277	1035	23.2	50	1	3	2	20	21	-	2	32	42	6.4	3.3	1.1

Table 3

			La	Ce	Pr	Nd	Sm	Eu	Gd	Tb	Dy	Ho	Er	Tm	Yb	Lu	∑REE	La/Y	Ce/Ce*	Eu/Eu*	$(La/Yb)_N$	$(Gd/Yb)_N$
Samples	Horizon ID	dl :	0.1	0.1	0.02	0.1	0.03	0.02	0.05	0.01	0.05	0.01	0.03	0.01	0.03	0.01						
MEI-09	M2b		80.6	135	14.5	47.9	8.37	2.12	6.27	0.82	4.04	0.68	1.56	0.23	1.35	0.17	303.66	5.68	0.94	0.84	6.49	3.72
MEI-08	M2b		219	248	37.5	107.5	16.3	3.82	10.35	1.36	7.19	1.23	2.78	0.36	2.04	0.27	657.70	9.95	0.65	0.85	11.67	4.06
MEI-07	M1b		420	516	77.2	256	42.8	9.91	28.8	3.41	17.1	2.47	5.07	0.5	2.23	0.26	1381.75	8.70	0.68	0.81	20.47	10.33
MEI-06	M1b		128.5	147.5	21.1	61.7	8.96	1.72	5.05	0.67	3.47	0.56	1.39	0.19	1.27	0.17	382.25	10.62	0.67	0.74	11.00	3.18
BAS-MEI			69.8	126	14.3	53.2	10.25	2.95	8.57	1.11	6.09	1.05	2.65	0.36	1.98	0.28	298.59	2.62	0.95	0.91	3.83	3.46
MEI-05	M2g		88.1	157.5	15.7	50.3	8.01	1.69	5.58	0.73	3.74	0.72	2.05	0.28	2.00	0.30	336.70	5.58	1.01	0.73	4.79	2.23
MEI-04	M2g		91.2	140	15.5	50.5	8.32	1.75	6.69	0.8	4.04	0.73	1.95	0.28	1.72	0.27	323.75	6.08	0.89	0.68	5.76	3.11
MEI-03	M2g		86	115.5	14.8	50.1	8.44	1.57	5.77	0.71	3.51	0.59	1.54	0.23	1.56	0.25	290.62	6.83	0.77	0.65	5.99	2.96
MEI-02	M1g		217	152	36.2	98.7	11.05	1.6	4.26	0.47	2.45	0.43	1.07	0.15	0.99	0.16	526.53	26.79	0.41	0.67	23.82	3.44
MEI-01	M1g		85.1	98.9	15.7	53.9	8.37	1.48	4.83	0.58	2.67	0.43	1.05	0.15	0.87	0.13	274.16	10.25	0.64	0.67	10.63	4.44
GRA-MEI			103.5	181	18.15	55.5	7.8	1.17	5.13	0.56	3.2	0.55	1.36	0.19	1.15	0.16	379.42	7.34	0.99	0.53	9.78	3.57